Analytical solutions of the block-diagonalized Hamiltonian for strained wurtzite semiconductors

M. Kumagai
NTT Basic Research Laboratories, 3-1 Morinosato Wakamiya, Atsugi, 243-01, Japan

S. L. Chuang
Department of Electrical and Computer Engineering, University of Illinois at Urbana-Champaign, 1406 West Green Street, Urbana, Illinois 61801

H. Ando
NTT Basic Research Laboratories, 3-1 Morinosato Wakamiya, Atsugi, 243-01, Japan

(Received 24 October 1997)

Analytical solutions using a recently derived block-diagonalized Hamiltonian for strained wurtzite crystals are shown. The theoretical results are used to extract the deformation potentials from the experimental results of the *A*-, *B*-, and *C*-line exciton transition energies as a function of the *c*-axis strain using a set of recently reported elastic stiffness constants. The obtained parameters are then applied to calculate the wave functions, valence band energies, effective masses, optical-momentum matrix elements, exciton Bohr radius, and binding energy as a function of strain. These analytical and numerical results are useful for understanding the optical and electronic properties near the band edges of strained wurtzite crystals. [S0163-1829(98)01224-7]

I. INTRODUCTION

Gallium nitride (GaN) and related materials have received a lot of attention recently. Theoretical models for the electrical and optical properties of GaN related materials play an important role in designing quantum-well structures for investigating physical processes as well as device applications using these wurtzite crystals. Blue-green semiconductor lasers using InGaN/GaN quantum-well structures have been successfully demonstrated[1,2] although the lifetime of these devices at room temperature is still limited.

The GaN materials are usually grown on substrates such as sapphire or SiC and a significant amount of strain exists. Since strain significantly affects the electronic and optical properties of semiconductors, it has been difficult to determine many of the band structure parameters due to an unknown amount of residual strain in many earlier samples. Although theoretical work on wurtzite crystals has been developed since the 1960s,[3] more experimental data on high-quality GaN and InGaN wurtzite crystals with measured strain values were available only recently. Many parameters such as the effective band structure parameters for the valence bands, the crystal field split-off energy, and the spin-orbit energy were obtained theoretically although not all of them match closely to the experimental data.

Theoretical models for wurtzite electronic structures with strain effects have been reported based on the $\boldsymbol{k}\cdot\boldsymbol{p}$ method.[3–8] A consistent set of basis functions with the corresponding Hamiltonian has been derived, and it has been found that the six-by-six Hamiltonian for the valence bands can be block-diagonalized into two three-by-three Hamiltonians.[6,7]

In this paper, we present analytical solutions and numerical results for the electronic band structures and wave functions for strained GaN bulk samples using the block-diagonalized Hamiltonian. Our calculations show the strain-dependent band mixing features of the GaN valence bands. Furthermore, analytical expressions for the strain dependence of the effective masses, exciton properties, and other important parameters of GaN have been calculated. These expressions will be useful for understanding the physical properties of GaN. Based on the analytical expressions, we obtain the deformation potentials using recent experimental data.[9]

In Sec. II, we derive the analytical expressions of the energy dispersion, wave functions, and other properties of the strained GaN. The deformation potentials are then extracted by using the analytical expressions of the interband transition energies for *A*-, *B*-, and *C*-line excitons. In Sec. III, numerical results for the strain effects on the valence wave functions, the energy dispersion, band-edge effective masses, and optical-matrix elements are shown. The strain-dependent exciton binding energies are also calculated. We then conclude in Sec. IV.

II. THEORY

In this section, we present the analytical solutions of the valence band energies and their corresponding eigenfunctions for the strained wurtzite semiconductors based on the recently developed block-diagonalized Hamiltonians. The analytical expressions of the band-edge effective masses, exciton properties, and optical matrix elements of the strained wurtzite semiconductors are also shown.

A. Block-diagonalized Hamiltonian and eigenenergies

The 6×6 valence band Hamiltonian for the strained wurtzite semiconductor can be blockdiagonalized into two 3×3 matrices[6,7]

$$H^{v}(\mathbf{k})=\begin{bmatrix} H^{U}_{3\times3}(\mathbf{k}) & 0 \\ 0 & H^{L}_{3\times3}(\mathbf{k}) \end{bmatrix}, \tag{1}$$

where

$$H^U_{3\times3}(\mathbf{k})=\begin{bmatrix} F & K_t & -iH_t \\ K_t & G & \Delta-iH_t \\ iH_t & \Delta+iH_t & \lambda \end{bmatrix}, \tag{2}$$

$$H^L_{3\times3}(\mathbf{k})=\begin{bmatrix} F & K_t & iH_t \\ K_t & G & \Delta+iH_t \\ -iH_t & \Delta-iH_t & \lambda \end{bmatrix}, \tag{3}$$

and the basis functions are shown in the Appendix. The matrix elements are

$$F=\Delta_1+\Delta_2+\lambda+\theta,$$

$$G=\Delta_1-\Delta_2+\lambda+\theta,$$

$$\lambda=\frac{\hbar^2}{2m_0}(A_1k_z^2+A_2k_t^2)+D_1\epsilon_{zz}+D_2(\epsilon_{xx}+\epsilon_{yy}),$$

$$\theta=\frac{\hbar^2}{2m_0}(A_3k_z^2+A_4k_t^2)+D_3\epsilon_{zz}+D_4(\epsilon_{xx}+\epsilon_{yy}), \tag{4}$$

$$K_t=\frac{\hbar^2}{2m_0}A_5k_t^2,$$

$$H_t=\frac{\hbar^2}{2m_0}A_6k_tk_z,$$

$$\Delta=\sqrt{2}\Delta_3,$$

and

$$k_t^2=k_x^2+k_y^2. \tag{5}$$

Here A_i's are the valence band effective-mass parameters which are similar to the Luttinger parameters in zinc blende crystal. D_is are the deformation potentials for wurtzite crystals.[3] In the above Hamiltonian, we have considered a strained-layer wurtzite crystal pseudomorphically grown along the (0001) direction (c axis), the only nonvanishing elements are[7]

$$\epsilon_{xx}=\epsilon_{yy}=\frac{a_0-a}{a},$$

$$\epsilon_{zz}=-\frac{2c_{13}}{c_{33}}\epsilon_{xx}, \tag{6}$$

where a_0 and a are the lattice constants of the substrate and the layer materials, respectively.

It should be noted that the above convention gives a negative in-plane strain ($\epsilon_{xx}=\epsilon_{yy}<0$) and positive c-axis strain ($\epsilon_{zz}>0$) for a biaxial compressive strain. In the case of a biaxial tensile strain, we have a positive in-plane strain and negative c-axis strain. In this paper, the parameter ϵ_{zz} is used as the variable in our plots since it has been directly measured from x-ray diffraction for a few samples.[9]

The eigenequation for the valence band energy E for a given $\mathbf{k}$ vector is given by

$$H^U_{3\times3}(\mathbf{k})\begin{bmatrix} g_1 \\ g_2 \\ g_3 \end{bmatrix}=E\begin{bmatrix} g_1 \\ g_2 \\ g_3 \end{bmatrix}. \tag{7}$$

The eigenequation has three analytical solutions,[10] and they can be expressed as

$$E_1=(S_1+S_2)-\frac{C_2}{3},$$

$$E_2=-\frac{1}{2}(S_1+S_2)-\frac{C_2}{3}+\frac{i\sqrt{3}}{2}(S_1-S_2), \tag{8}$$

$$E_3=-\frac{1}{2}(S_1+S_2)-\frac{C_2}{3}-\frac{i\sqrt{3}}{2}(S_1-S_2),$$

where

$$q=\frac{1}{3}C_1-\frac{1}{9}C_2^2,$$

$$r=\frac{1}{6}(C_1C_2-3C_0)-\frac{1}{27}C_2^3, \tag{9}$$

$$S_1=[r+(q^3+r^2)^{1/2}]^{1/3},$$

$$S_2=[r-(q^3+r^2)^{1/2}]^{1/3}, \tag{10}$$

and

$$C_2=-(F+G+\lambda),$$

$$C_1=FG+G\lambda+F\lambda-\Delta^2-K_t^2-2H_t^2, \tag{11}$$

$$C_0=-\det[H^U_{3\times3}].$$

The lower 3×3 Hamiltonian is the complex conjugate of the upper 3×3 Hamiltonian. Therefore, they have exactly the same eigenvalues since the energies are real. The wave functions of the lower Hamiltonian are the complex conjugates of the corresponding wave functions of the upper Hamiltonian. Below we consider the solutions for the upper Hamiltonian.

B. Wave functions

After we obtain the three eigenvalues, we calculate the corresponding eigenfunctions. For a general k_t not at the zone center, the envelope functions are determined by

$$\begin{bmatrix} g_1^v \\ g_2^v \\ g_3^v \end{bmatrix}=\frac{1}{D^v}\begin{bmatrix} \{iH_t(G-E^v)+(\Delta-iH_t)K_t\} \\ \{-iH_tK_t-(\Delta-iH_t)(F-E^v)\} \\ \{(G-E^v)(F-E^v)-K_t^2\} \end{bmatrix}, \tag{12}$$

where

$$D^v=\sqrt{|iH_t(G-E^v)+K_t(\Delta-iH_t)|^2+|iH_tK_t+(\Delta-iH_t)(F-E^v)|^2+|(G-E^v)(F-E^v)-K_t^2|^2}, \tag{13}$$

for $v=$heavy hole (HH), light hole (LH), and crystal-field split-off hole (CH) bands. Care should be taken at $k_t=0$ in the above expressions.

Once we obtain the expansion coefficients g_1, g_2, and g_3, the complete Bloch wave function is given by

$$\Psi^v(\mathbf{r},\mathbf{k})=\frac{1}{\sqrt{V}}\,e^{i(\mathbf{k}\cdot\mathbf{r})}\sum_{i=1}^{3} g_i^v(\mathbf{k})|i\rangle \tag{14}$$

for each hole band v.

C. Band-edge energies and exciton transition energies

At the band edges, $k_t=k_z=0$, the Hamiltonians (2) and (3) can be simplified since $K_t=0$ and $H_t=0$. This Hamiltonian has three eigenvalues for the valence bands as shown in Fig. 1,

$$E_0^{\mathrm{HH}}=F_0,$$

$$E_0^{\mathrm{LH}}=\frac{G_0+\lambda_\epsilon}{2}+\sqrt{\left(\frac{G_0-\lambda_\epsilon}{2}\right)^2+\Delta^2}, \tag{15}$$

$$E_0^{\mathrm{CH}}=\frac{G_0+\lambda_\epsilon}{2}-\sqrt{\left(\frac{G_0-\lambda_\epsilon}{2}\right)^2+\Delta^2},$$

where

$$F_0=\Delta_1+\Delta_2+\lambda_\epsilon+\theta_\epsilon,$$

$$G_0=\Delta_1-\Delta_2+\lambda_\epsilon+\theta_\epsilon,$$

$$\lambda_\epsilon=D_1\epsilon_{zz}+D_2(\epsilon_{xx}+\epsilon_{yy}), \tag{16}$$

$$\theta_\epsilon=D_3\epsilon_{zz}+D_4(\epsilon_{xx}+\epsilon_{yy}).$$

For the conduction band, the band-edge energy is given by

$$E_0^C=\Delta_1+\Delta_2+E_g+P_{c\epsilon}, \tag{17}$$

which includes a hydrostatic energy shift

$$P_{c\epsilon}=a_{cz}\epsilon_{zz}+a_{ct}(\epsilon_{xx}+\epsilon_{yy}). \tag{18}$$

D. Band-edge effective masses and optical matrix elements

Band-edge effective masses can be obtained by setting either $k_t=0$ or $k_z=0$ in the three-by-three Hamiltonian and looking for the $E-k$ relation for a small k_z or k_t to find the zone center effective masses. We then obtain the transverse (perpendicular to the c axis) and z-directional (parallel to the c axis) effective masses, respectively.

These results can also be calculated by using near zone center $E-k$ dispersion relations and taking their second derivatives with respect to k_t and k_z at the zone center. The calculated results are summarized in Table I.

Optical-matrix elements for transverse (t) and c-axis (z) polarized waves are given by

$$M_z=|\langle\psi^c|p_z|\psi^v\rangle|^2,$$

$$M_t=|\langle\psi^c|p_t|\psi^v\rangle|^2, \tag{19}$$

respectively. These quantities determine the optical response of the materials for the TE (t) and TM (z) polarized light. The calculated analytical results are presented in Table II, where E_{pz} and E_{pt} are given by

$$E_{pz}=\frac{2}{m_0}|\langle iS|p_z|Z\rangle|^2,$$

$$E_{pt}=\frac{2}{m_0}|\langle iS|p_x|X\rangle|^2,$$

$$=\frac{2}{m_0}|\langle iS|p_y|Y\rangle|^2, \tag{20}$$

and p_z, p_x, and p_y are the z, x, and y components of the momentum operator.

E. Exciton Bohr radius and binding energy

The bound state of the exciton binding energy is often calculated using the variational method because of its simplicity. In axially symmetric crystals such as wurtzite, the variational wave function and the Hamiltonian are anisotropic. Here we employ the variational method[16] for the calculation of exciton binding energy and Bohr radius. The Hamiltonian for an electron-hole pair is given by

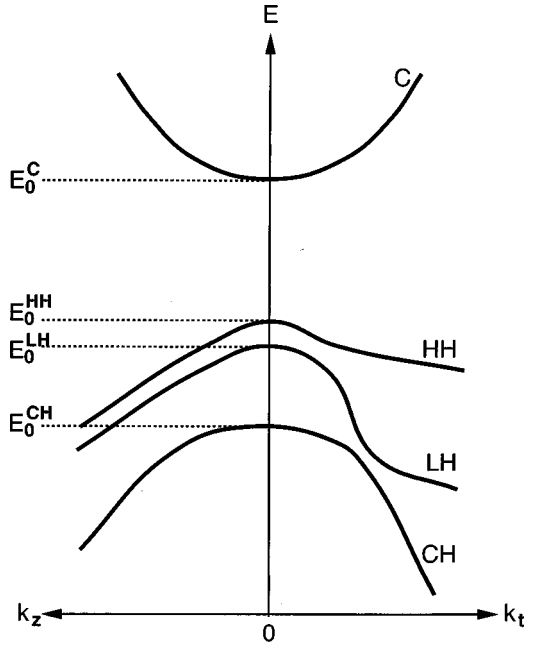

FIG. 1. Schematic diagram for the conduction (C), heavy-hole (HH), light-hole (LH), and crystal-field split-off hole (CH) bands of a strained wurtzite crystal.

$$H=-\frac{\hbar^2}{2\mu_t}\left(\frac{\partial^2}{\partial x^2}+\frac{\partial^2}{\partial y^2}\right)-\frac{\hbar^2}{2\mu_z}\frac{\partial^2}{\partial z^2}-\frac{e^2}{[\kappa_t\kappa_z(x^2+y^2)+\kappa_t^2z^2]^{1/2}}, \tag{21}$$

where μ_t and μ_z are the reduced mass in the t and z directions, respectively. These reduced effective masses are calculated from those of the valence bands and conduction band effective masses in the corresponding t and z directions. κ_t and κ_z are dielectric constants of the crystal for the t and z directions, respectively.

This Hamiltonian can be simplified by normalizing the energy and length by

$$E_0\equiv\frac{\mu_t e^4}{2\hbar^2\kappa_t\kappa_z},$$

$$a_0\equiv\frac{(\kappa_t\kappa_z)^{1/2}\hbar^2}{\mu_t e^2}, \tag{22}$$

yielding

$$H=-\left[\frac{\partial^2}{\partial x^2}+\frac{\partial^2}{\partial y^2}+\frac{\mu_t}{\mu_z}\frac{\partial^2}{\partial z^2}\right]-\frac{2}{[x^2+y^2+(\kappa_t/\kappa_z)z^2]^{1/2}}. \tag{23}$$

The variational function is assumed to be of the form for the ground $(1S)$ state,

$$\psi(\mathbf{r})=\frac{1}{\sqrt{\pi a_z a_t^2}}\exp\left[-\left(\frac{x^2+y^2}{a_t^2}+\frac{z^2}{a_z^2}\right)^{1/2}\right], \tag{24}$$

where a_t and a_z are the variational parameters and they are the effective Bohr radius for the t and z directions, respectively. Using the relation

$$(2\pi)^{-3/2}\int\int\int e^{-a|r|}e^{i\mathbf{k}\cdot\mathbf{r}}d^3\mathbf{r}=\sqrt{\frac{8}{\pi}}\frac{a}{(a^2+k^2)^2}, \tag{25}$$

we obtain the variational function in the Fourier transform domain

$$\Psi(\mathbf{r})=\frac{1}{\sqrt{\pi a_z a_t^2}}\int\int\int\frac{1}{\pi^2(k_t^2+k_z^2+1)^2}\times\exp\left(-\frac{i\mathbf{k}_t\cdot\mathbf{r}_t}{a_t}\right)\exp\left(-\frac{ik_z z}{a_z}\right)d^3\mathbf{k}, \tag{26}$$

where $\mathbf{r}_t=(x,y)$ and $\mathbf{k}_t=(k_x,k_y)$.

Using the above variational function and minimizing the energy expectation value, we obtain the exciton binding energy

$$E_{\text{bind}}=\frac{1}{3a_t^2}\left(2+\frac{\omega}{1+\alpha^2}\right)-\frac{2}{a_t a_z}\sinh^{-1}\alpha \tag{27}$$

and the corresponding transverse direction exciton Bohr radius

$$a_t=\frac{1}{3}\left(2+\frac{\omega}{1+\alpha^2}\right)\frac{\alpha}{\sinh^{-1}\alpha}, \tag{28}$$

where the parameters ω and α are defined as

$$\omega\equiv\frac{\mu_t}{\mu_z}\frac{\kappa_t}{\kappa_z}, \tag{29}$$

$$a_z=a_t\sqrt{\frac{\kappa_z}{\kappa_t}(1+\alpha^2)}. \tag{30}$$

The z-directional exciton Bohr radius is obtained using the calculated a_t value and Eq. (30).

Note that our simplified variational approach ignores the valence band-mixing effects on exciton states. The band-mixing effects in the presence of strain will further complicate the exciton binding energies, especially those of the unbound states due to strong coupling of the bands. For the ground $1S$ states excitons, the variational approach should give a resonably accurate estimation of the binding energies as have been demonstrated in zinc blende systems such as GaAs.

F. Exciton transition energy and extraction of the deformation potentials

The A-, B-, and C-line exciton transition energies are obtained from the conduction band to the HH, LH, and CH band transition energies minus the corresponding exciton binding energies

$$E_A=E_0^C-E_0^{\text{HH}}-E_{\text{bind}}^{\text{HH}},$$

$$E_B=E_0^C-E_0^{\text{LH}}-E_{\text{bind}}^{\text{LH}}, \tag{31}$$

$$E_C=E_0^C-E_0^{\text{CH}}-E_{\text{bind}}^{\text{CH}},$$

where E_{bind}^{v} stands for the exciton binding energies calculated from Eq. (27) for the conduction band to three v-band hole bands transitions. We need to estimate the deformation potentials for calculating the strain effects in wurtzite semiconductors. There are four deformation potentials D_1 to D_4 for the valence bands, and two deformation potentials a_{ct} and a_{cz} for the conduction band.

First we adopt the quasicubic approximation[3] to reduce the number of unknowns:

$$A_1-A_2=-A_3=2A_4,$$

$$A_3+4A_5=\sqrt{2}A_6,$$

$$\Delta_2=\Delta_3, \tag{32}$$

$$D_1-D_2=-D_3=2D_4.$$

From this approximation, we can reduce two unknown valence band deformation potentials. Furthermore, we ignore the anisotropic property of the conduction band deformation potentials

$$a_{cz}=a_{ct}=a_c. \tag{33}$$

TABLE I. Band-edge effective masses.

Valence band	m_z/m_0	m_t/m_0
HH	$-(A_1+A_3)^{-1}$	$-(A_2+A_4)^{-1}$
LH	$-\left[A_1+\left(\frac{E_0^{LH}-\lambda_\epsilon}{E_0^{LH}-E_0^{CH}}\right)A_3\right]^{-1}$	$-\left[A_2+\left(\frac{E_0^{LH}-\lambda_\epsilon}{E_0^{LH}-E_0^{CH}}\right)A_4\right]^{-1}$
CH	$-\left[A_1+\left(\frac{E_0^{CH}-\lambda_\epsilon}{E_0^{CH}-E_0^{LH}}\right)A_3\right]^{-1}$	$-\left[A_2+\left(\frac{E_0^{CH}-\lambda_\epsilon}{E_0^{CH}-E_0^{LH}}\right)A_4\right]^{-1}$

Ignoring the strain-dependent variation of the exciton binding energies which is small [less than 0.8 meV as will be shown later in Fig. 10(b)], we obtain the following linear coefficients for the slopes of the A-, B-, and C-line exciton energies as a function of the c-axis strain ϵ_{zz}:

$$S_A=(a_c-D_2)\left(1-\frac{c_{33}}{c_{13}}\right)+\frac{c_{33}}{c_{13}}D_4,$$

$$S_B=(a_c-D_2)\left(1-\frac{c_{33}}{c_{13}}\right)+\frac{c_{33}}{c_{13}}D_4, \tag{34}$$

$$S_C=(a_c-D_2)\left(1-\frac{c_{33}}{c_{13}}\right)-2D_4$$

as shown in Fig. 2. Knowing the slopes S_A and S_C from the large compressive strain region of the A-line exciton and C-line exciton transition energies, we obtain (a_c-D_2) and D_4.

From Eqs. (31) we obtain the following relation if we ignore the slight difference of the HH and LH exciton binding energies:

$$E_B-E_A=\frac{\Delta_1+3\Delta_2}{2}+\frac{\theta_\epsilon}{2}-\sqrt{\left(\frac{\Delta_1-\Delta_2+\theta_\epsilon}{2}\right)^2+2\Delta_3^2}, \tag{35}$$

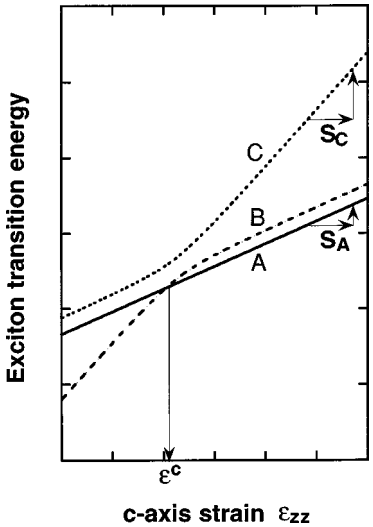

FIG. 2. Theoretical curves for the A-, B-, and C-line exciton transition energies are plotted as a function of the c-axis strain with their linear slopes in the compressive strain region.

with

$$\theta_\epsilon=D_3\epsilon_{zz}+D_4(\epsilon_{xx}+\epsilon_{yy})=\left(D_3-\frac{c_{33}}{c_{13}}D_4\right)\epsilon_{zz}. \tag{36}$$

From the strain value of the crossing point ϵ^c between E_A and E_B from Fig. 2, we can calculate the quantity $D_3-(c_{33}/c_{13})D_4$, which can be used as a check to confirm the obtained deformation potential values from the previous procedure. We assume that

$$a_c=\frac{1}{2}a, \tag{37}$$

where the total value a for the interband deformation potential is obtained from the hydrostatic pressure measurement.[14] Therefore, we can extract all the deformation potentials from the experimental data following the theoretical curves shown in Fig. 2.

III. NUMERICAL RESULTS AND COMPARISON WITH EXPERIMENTAL RESULTS

A. Extraction of deformation potentials

The procedure described in Sec. II is used to obtain the deformation potentials by comparing the theoretical results with the experimental data.[9] Since the extracted deformation potentials depend on the elastic constants, we take the elastic constants from recently measured values in Ref. 15. The extracted deformation potentials and other theoretical band structure parameters are listed in Table III. In Fig. 3(a), we show our calculated exciton transition energies for the A-, B-, and C-line excitons and the experimental results by Shi-

TABLE II. Interband optical momentum matrix elements.

Valence band	M_z	M_t
HH	0	$\frac{m_0}{4}E_{pt}$
LH	$\frac{E_0^{CH}-\lambda_\epsilon}{E_0^{CH}-E_0^{LH}}\left(\frac{m_0}{2}E_{pz}\right)$	$\frac{E_0^{LH}-\lambda_\epsilon}{E_0^{LH}-E_0^{CH}}\left(\frac{m_0}{4}E_{pt}\right)$
CH	$\frac{E_0^{LH}-\lambda_\epsilon}{E_0^{LH}-E_0^{CH}}\left(\frac{m_0}{2}E_{pz}\right)$	$\frac{E_0^{CH}-\lambda_\epsilon}{E_0^{CH}-E_0^{LH}}\left(\frac{m_0}{4}E_{pt}\right)$
Sum	$\frac{m_0}{2}E_{pz}$	$\frac{m_0}{2}E_{pt}$

TABLE III. Physical parameters of GaN.

Parameter	Value	References
Lattice constant (Å)		11
a	3.189	
c	5.185	
Energy parameters		
E_g (300 K) (eV)	3.44	12
$\Delta_{cr}=\Delta_1$ (meV)	22.0	9
$\Delta_{so}=3\Delta_2$ (meV)	15.0	9
$\Delta_3=\Delta_2$ (meV)	5.0	
Conduction band effective masses		4
m_e^z/m_0	0.20	
m_e^t/m_0	0.18	
Valence band effective mass parameters		4
A_1	−6.56	
A_2	−0.91	
A_3	5.65	
A_4	−2.83	
A_5	−3.13	
A_6	−4.86	
Deformation potentials (eV)		
a (interband)	−9.20	14
$a_c=\frac{1}{2}a$ (conduction band)	−4.60	this work
D_1	−1.70	this work
D_2	6.30	this work
D_3	8.00	this work
D_4	−4.00	this work
Dielectric constants		9
κ_t	7.87	
κ_z	8.57	
Elastic stiffness constants (10^{11} dyn/cm^2)		15
c_{11}	39.0	
c_{12}	14.5	
c_{13}	10.6	
c_{33}	39.8	
c_{44}	10.5	
c_{66}	12.3	

kanai *et al.*[9] We use a constant value of 26 meV for the exciton binding energy in the calculation of the interband transition energies. The strain dependence of the exciton binding energies is negligible due to their small variations [less than 0.8 meV as will be shown later in Fig. 10(b)]. We can see that the agreement between the theoretical results and the experimental data is very good.

Both the calculated and experimental results show the linear dependence of the exciton transition energies on the strain ϵ_{zz} in most of the strain regions except near the anticrossing between the LH and CH bands at a slightly biaxial tensile (negative ϵ_{zz}) strain region. The anticrossing between the LH and CH bands near the -0.07% strain shows a strong coupling of the LH and CH bands and the exchange nature of their wave functions.

Figure 3(b) gives the transition energy difference between B- and A-line excitons, as well as C- and A-line excitons. We can see that in the large biaxial compressive strain case, the energy difference E_B-E_A approaches a constant value and the slope is zero since $S_A=S_B$. Therefore, these measurements are very useful for determining the experimental values of the deformation potentials.

B. Energy band structures

The valence-band mixing effects can be understood from the dispersion relations and corresponding wave functions of the HH, LH, and CH bands. Figures 4(a)–4(d) show the calculated valence band dispersion relations of bulk GaN for (a) a biaxial compressive strain $\epsilon_{zz}=0.2\%$, (b) zero strain 0%, (c) a small biaxial tensile strain -0.09%, and (d) a large biaxial tensile strain -0.2%. We plot the three valence bands: heavy hole (HH), light hole (LH), and crystal-field split-off hole (CH) bands along the k_t and k_z directions.

Along the k_z direction ($k_t=0$) on the left side of Figs. 4(a)–4(d), the Hamiltonian is of the form

$$H_{3\times3}^{U}(\mathbf{k})=\begin{bmatrix} F_z & 0 & 0 \\ 0 & G_z & \sqrt{2}\Delta_3 \\ 0 & \sqrt{2}\Delta_3 & \lambda_z \end{bmatrix}, \tag{38}$$

where F_z, G_z, and λ_z are obtained from F, G, and λ by setting $k_t=0$. Clearly the g_1 component of the Hamiltonian is decoupled from the g_2 and g_3 components. The HH band has a purely parabolic dispersion, $E=F_z$, along the k_z direction for all strain cases. On the other hand, the g_2 and g_3 components are coupled to each other due to the off-diagonal elements $\sqrt{2}\Delta_3$. For the zero strain and the biaxial compressive strain cases, the LH and CH bands are far apart, and their coupling due to this off-diagonal term becomes relatively small. Therefore, the LH and CH bands appear to be parabolic along the k_z direction as shown in Figs. 4(a) and 4(b). For a tensile strain case, however, the diagonal terms G_z and λ_z become close and the coupling due to the off-diagonal elements becomes significant. Therefore, the non-parabolic nature of the LH and CH bands along the k_z direction appears as shown in Figs. 4(c) and 4(d).

On the right half of Figs. 4(a)–4(d), the dispersion relations along the k_t direction ($k_z=0$) are plotted, and their behavior can be understood as follows. The Hamiltonian takes the form

$$H_{3\times3}^{U}(\mathbf{k})=\begin{bmatrix} F_t & K_t & 0 \\ K_t & G_t & \sqrt{2}\Delta_3 \\ 0 & \sqrt{2}\Delta_3 & \lambda_t \end{bmatrix}, \tag{39}$$

where F_t, G_t, and λ_t are obtained from F, G, and λ by setting $k_z=0$.

It can be seen from the Hamiltonian, that the HH, LH, and CH bands are coupled to each other along the k_t direction, and all three bands become non-parabolic as shown in Figs. 4(a)–4(d). In the compressive and zero strain case, Figs. 4(a) and 4(b), the coupling between CH band and other two bands is weak at a small k_t.

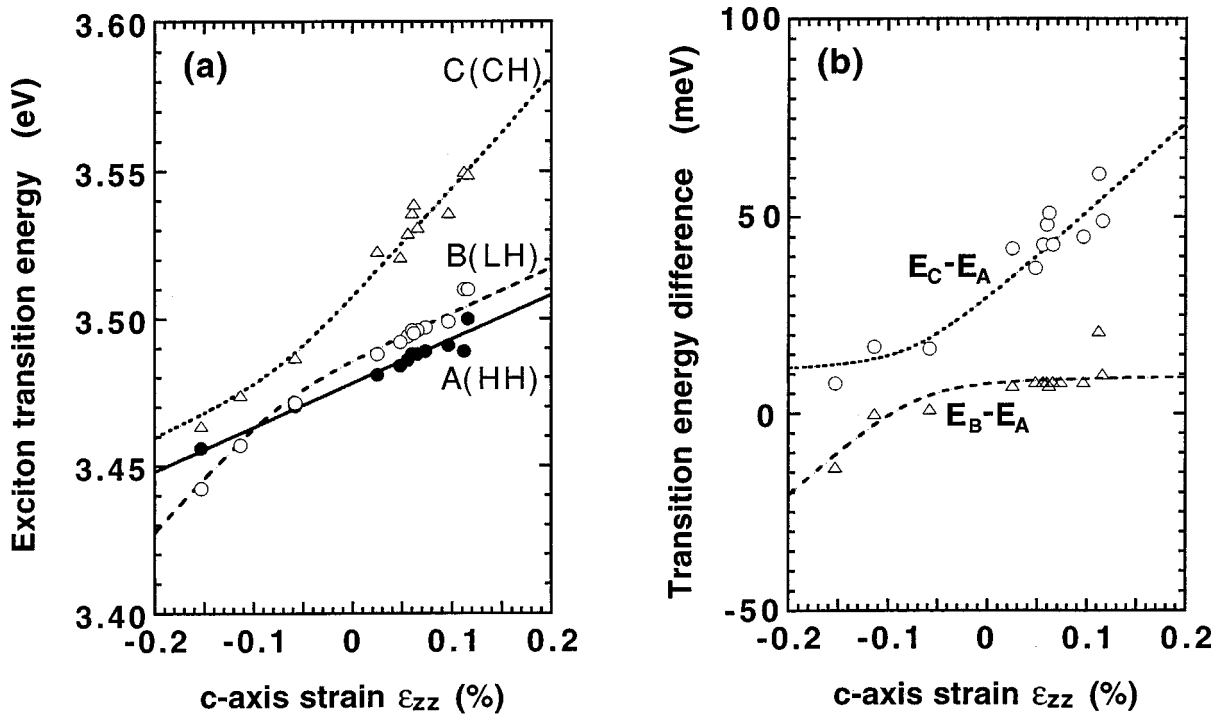

FIG. 3. (a) Theoretical values for the exciton transition energies are compared with the experimental data (symbols) for the *A*-, *B*-, and *C*-line excitons. (b) The differences of the *C*-line and *A*-line as well as *B*-line and *A*-line exciton transition energies are plotted as a function of the *c*-axis strain.

It should be noted that even in the zero strain case, all three bands are not degenerate at the zone center for wurtzite crystals. This feature is different from that of the cubic III-V semiconductors, for which the HH and LH bands have the same energy at the zone center, and they split in the presence of strain. Therefore, the unstrained wurtzite crystal is similar to a prestrained zinc blende crystal. Adding the strain to the wurtzite crystal causes either further splittings or reduced splittings among some of the bands depending on whether the strain is compressive or tensile.

It is interesting to note that the HH and LH bands are degenerate at the zone center at a certain tensile strain value [$\epsilon_{zz} \simeq -0.09\%$, Fig. 4(c)], and the band structure resembles that of an unstrained zinc blende crystal. If the tensile strain is increased above that value, the LH band is lifted to the top of the valence band.

C. Wave functions

In addition to the band structure dispersions, the wave functions for the wurtzite crystals show interesting features on the band mixing. However, little work has been done so far to understand the wave functions of the wurtzite crystals. In Figs. 5–7, we show the wave functions of the three valence bands of compressive strained, unstrained, and tensile strained wurtzite GaN crystals, respectively, using the new three-by-three Hamiltonian. In our calculation, the vth valence band wave function with a wave vector $\mathbf{k}$ is determined by the eigenfunction of Eq. (7). The mixing ratio of the coefficients g_1, g_2, and g_3 determines the nature of each band.

First, we consider the wave functions for the band structure along the k_z direction. Since the HH band is decoupled from the LH and CH bands, we obtain $g_1=1$ and $g_2=g_3=0$ for the HH band as shown in the left half of Figs. 5(a), 6(a), and 7(a), and $g_1=0$ for the LH and CH bands as shown in Figs. 5(b) and 5(c), 6(b) and 6(c), and 7(b) and 7(c). For LH and CH bands, the LH and CH band wave functions consist of a mixture of the g_2 and g_3 components along the k_z direction. This is the direct consequence of the block-diagonalized form of the Hamiltonian (2). Along this direction, only the mixing of the g_2 and g_3 components is needed to know the wave functions.

For a biaxial compressive strain value, $\epsilon_{zz}=0.2\%$, Figs. 5(b) and 5(c) show that near the zone center along the k_z direction, the LH band is dominated by the g_2 component with a small amount of mixing with the g_3 component. Similarly, the CH band is dominated by the g_3 component with a small amount of mixing with the g_2 component. Apart from the zone center, the mixing effects approach zero. Therefore, the HH, LH, and CH bands are virtually independent of each other and have nearly pure nature of g_1, g_2, and g_3 components along the k_z direction when the applied strain is increasingly compressive.

On the other hand, strong mixing between g_2 and g_3 along the k_z direction for the LH and CH bands exists for the biaxial tensile strain case, as shown in Figs. 7(b) and 7(c). Near the zone center, the LH and CH bands have a dominant g_3 or g_2 component, respectively. In the large k_z region, the LH and CH bands exchange their dominant components, g_3 to g_2 and g_2 to g_3, respectively.

Along the k_t direction, the mixing between all three components exists. For the compressive strain case on the right side of Figs. 5(a)–5(c), the coupling between g_1 and g_2 occurs gradually in the small k_t region (less than 0.04 Å^{-1}),

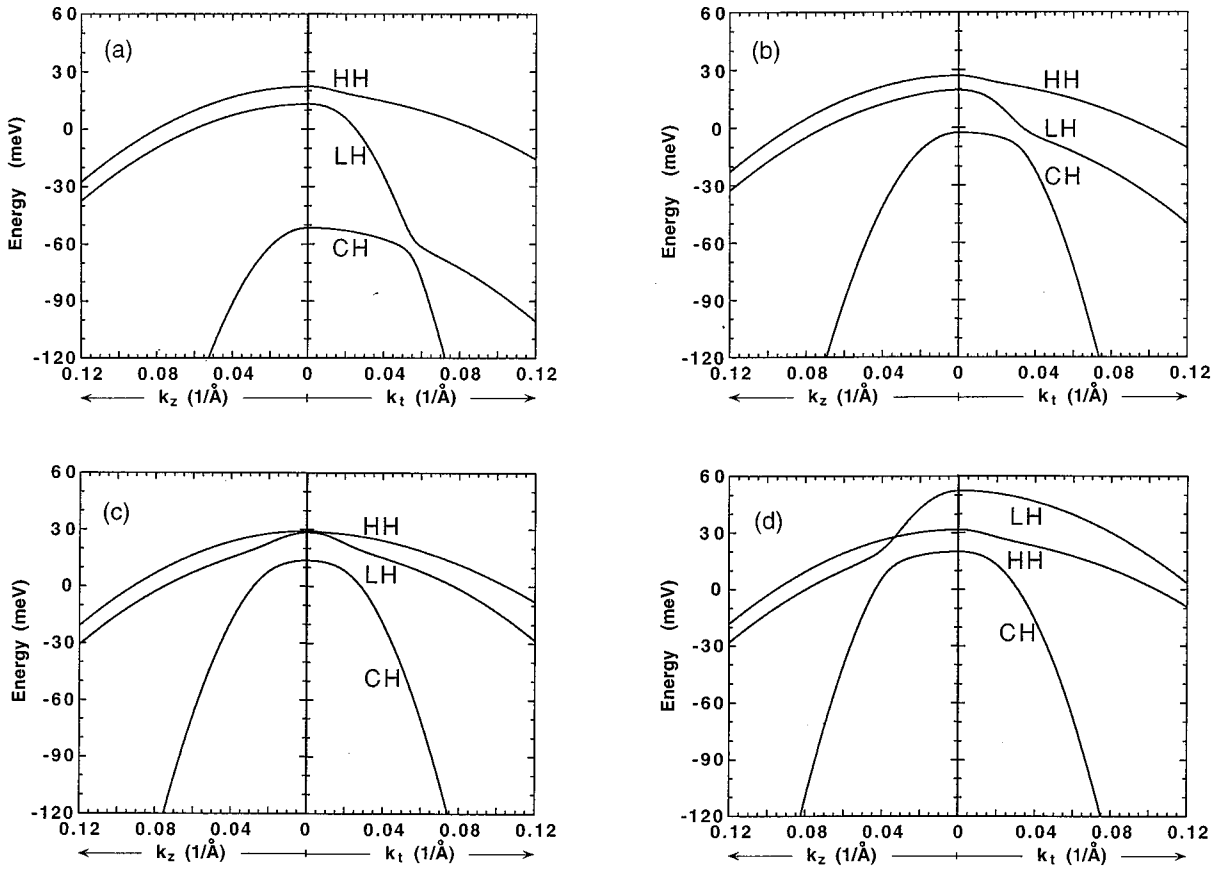

FIG. 4. The valence band structures of the heavy-hole (HH), light-hole (LH), and crystal-field split-off hole (CH) bands are plotted for (a) a biaxial compressive strain $\epsilon_{zz}=0.2\%$, (b) zero strain 0%, (c) a small biaxial tensile strain -0.09%, and (d) a large biaxial tensile strain -0.2%

and the coupling saturates in the large k_t region for the HH band as shown in Fig. 5(a). The coupling of g_1 with g_2 and g_3 shows more drastic effects for the LH and CH bands as shown in Figs. 5(b) and 5(c), especially near $k_t=0.06$ Å^{-1}. Also in the band dispersion curve in Fig. 4(a), we can see the anticrossing behavior of the LH and CH bands. This anticrossing behavior of the LH and CH bands occurs at a smaller value of k_t for the unstrained case than that of the compressive strain case, as shown on the right sides of Figs. 6(b) and 6(c), although the general mixing features are similar to those of the compressive strain case.

On the other hand, for a biaxial tensile strain case the general mixing of all three components is clear as shown in Figs. 7(a)–7(c), but less dramatic than the anticrossing behaviors of the unstrain and compressive strain cases. As a matter of fact, the LH band is dominated by the g_3 component while the CH band is a mixture of g_1 and g_2.

D. Band-edge effective masses and optical momentum matrix elements

The band-edge effective masses play an important role in determining the optical properties near the band gap. The strain dependence of the band-edge effective masses is useful for the understanding of optical processes such as gain and absorption spectrum as well as electronic transport processes. In Fig. 8 we plot the calculated valence band effective masses near the band edges. It can be seen that the effective masses for all bands are heavy along the k_t and k_z directions. A large anisotropy is also observed. The HH band-edge effective masses along the k_z and k_t directions are constant (about $1.1m_0$ and $0.3m_0$, respectively) independent of the strain. In contrast, the LH and CH band-edge effective masses depend on the strain. For a large compressive strain, the LH band-edge effective masses approach those of the HH bands, and CH-band effective masses become heavy in the k_t direction, and light along the k_z direction. For a large tensile strain, the situation is reversed, and the CH band-edge effective masses approach those of the HH bands. At a -0.05% tensile strain, the LH band effective masses along the k_z and k_t directions are equal. For the CH band, equal effective masses are realized at -0.1% tensile strain. It is also seen that the LH and CH band effective masses are equal at a biaxial tensile strain of -0.07%.

From the band-edge wave functions and energies, we calculate the optical momentum matrix elements of GaN, which are important for the interband optical transitions. The results are plotted in Fig. 9 as a function of the c-axis strain. Under a biaxial compressive strain (negative $\epsilon_{xx}=\epsilon_{yy}$ and positive ϵ_{zz}), the interband optical matrix elements for the HH and LH bands to the conduction band transitions are dominated by the transverse polarization (on the x-y plane perpendicular to the c-axis). On the other hand, interband transitions between the CH band and the conduction band are dominated by the polarization along the c axis (z axis). Under a

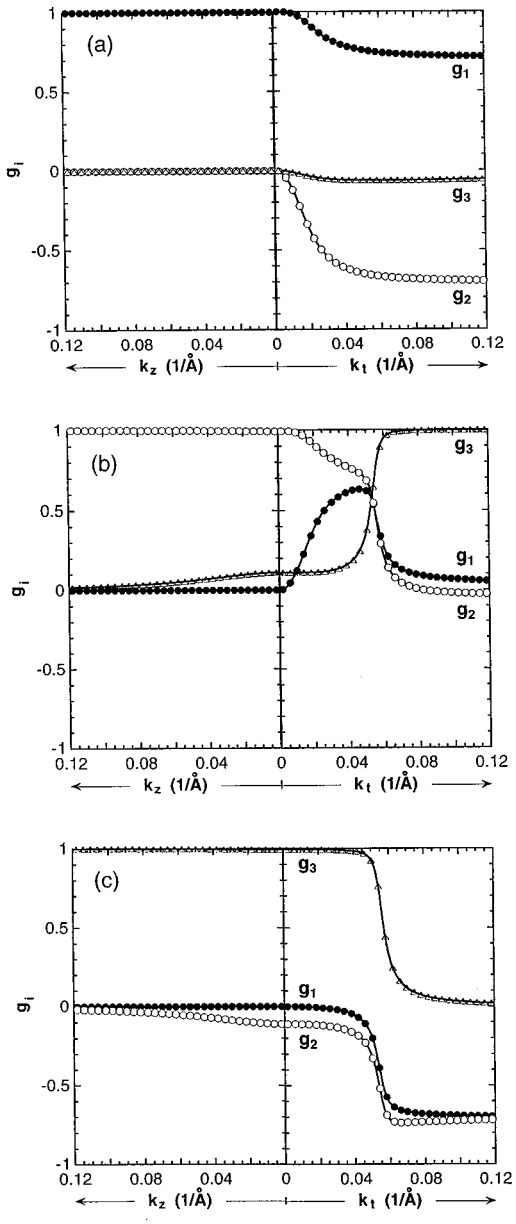

FIG. 5. The three components of the wave functions g_1, g_2, and g_3 are plotted along the k_t and k_z directions for (a) the heavy-hole (HH), (b) the light-hole (LH), and (c) the crystal-field split-off hole (CH) bands. The strain is biaxial compressive with $\epsilon_{zz} = 0.2\%$.

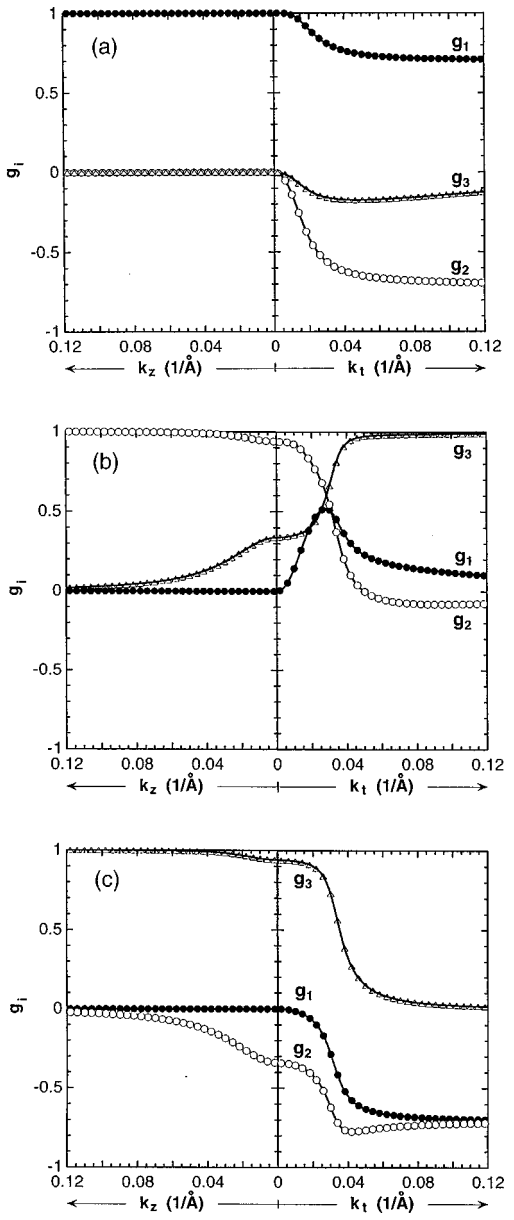

FIG. 6. The three components of the wave functions g_1, g_2, and g_3 are plotted along the k_t and k_z directions for (a) the heavy-hole (HH), (b) the light-hole (LH), and (c) the crystal-field split-off hole (CH) bands. The strain is zero.

tensile strain, however, the LH and CH bands switch their polarization dependencies because of their anticrossing behavior as a function of strain. The HH band has constant momentum matrix elements independent of the strain, and the z-polarized component is always 0. These anisotropic optical transition rules can be used in optical measurements such as photoluminescence, photoreflectance, and absorption near the band edges.

E. Exciton Bohr radius and binding energy

Using the above band-edge effective masses, we then calculate the excitonic properties including the exciton Bohr radius and binding energy. In wide gap materials, excitons play an important role due to their large Coulombic interaction caused by small dielectric constants and large effective masses.

The exciton Bohr radius and binding energy are calculated by using the anisotropic variational function. The results are shown in Fig. 10. In general, the exciton Bohr radii are small (less than 40 Å), and the binding energies are large (more than 25 meV) compared with those of the GaAs materials. It can be seen from Fig. 10(a) that the anisotropic Bohr radius parameters, a_t and a_z of the HH to conduction band exciton (or A-line exciton) are independent of the strain, and a_z is larger than a_t. For the LH band to conduction band exciton (B-line exciton), both a_z and a_t approach those of the HH band exciton asymptotically when we increase the compressive strain. For a large tensile strain, the LH band exciton is squeezed in the z direction and elongated

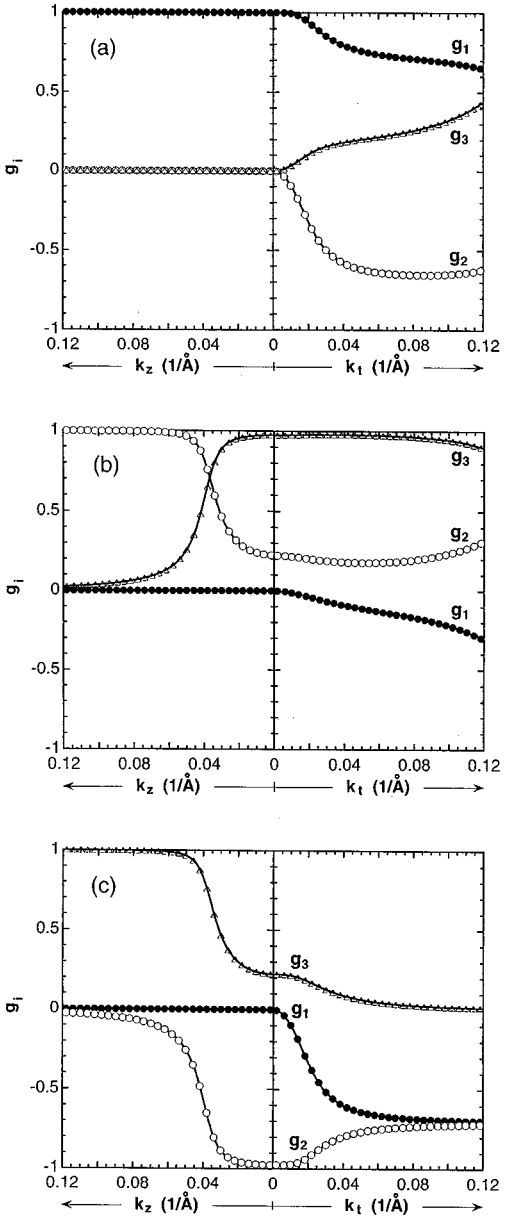

FIG. 7. The three components of the wave functions g_1, g_2, and g_3 are plotted along the k_t and k_z directions for (a) the heavy-hole (HH), (b) the light-hole (LH), and (c) the crystal-field split-off hole (CH) bands. The strain is biaxial tensile with $\epsilon_{zz}=-0.2\%$.

along the t direction. However, for the CH to conduction band exciton (C-line exciton), the situation is the opposite of the B-line exciton.

Figure 10(b) shows the strain dependence of the exciton binding energies for the A-, B-, and C-line excitons of wurtzite GaN crystals. The values vary between 25.4 and 26.2 meV, and they are larger than that of GaAs (4.2 meV). The difference between the maximum value and the minimum value is less than 1 meV (4%). The binding energy of the HH-band exciton is constant due to the constant nature of its band-edge effective masses. The LH-band and CH-band excitons reach a minimum at -0.06 and $-0.09\,\%$ tensile strain, respectively. These strain values correspond to those of the isotropic effective mass conditions.

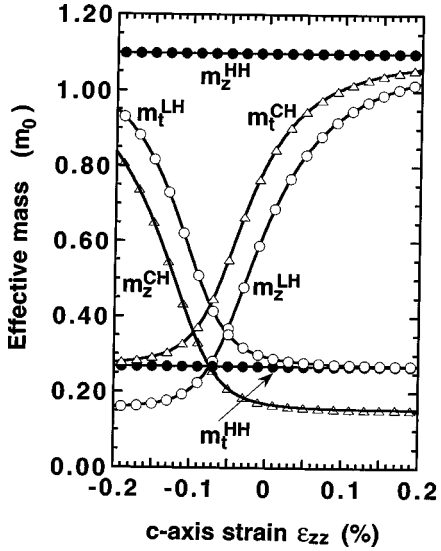

FIG. 8. The band-edge effective masses of the HH, LH, and CH bands along the k_t and k_z directions are plotted as a function of the c-axis strain.

IV. CONCLUSIONS

We have derived the full analytical expressions of the bulk wave function and energy dispersion of the strained wurtzite GaN using a recently block-diagoinalized Hamiltonian. Based on the analytical expressions, we have extracted the deformation potentials from experimental exciton transition energies as a function of the c-axis strain. Numerical results of the energy band dispersion, wave functions, effective masses, optical matrix elements, and exciton properties are shown for the biaxial compressive, tensile, and zero strain cases. These calculations also describe quantitatively the strain-dependent band-mixing features of the wurtzite GaN materials. These analytical expressions and numerical examples will be useful for understanding the band-

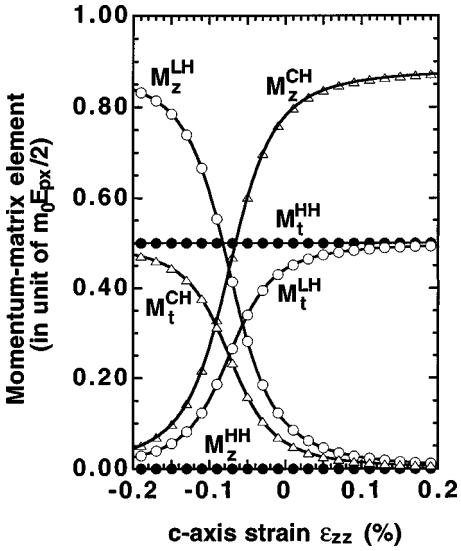

FIG. 9. The interband optical momentum matrix elements of the HH, LH, and CH bands to the conduction band transitions and their polarization dependencies (t or z polarized) are plotted as a function of the c-axis strain.

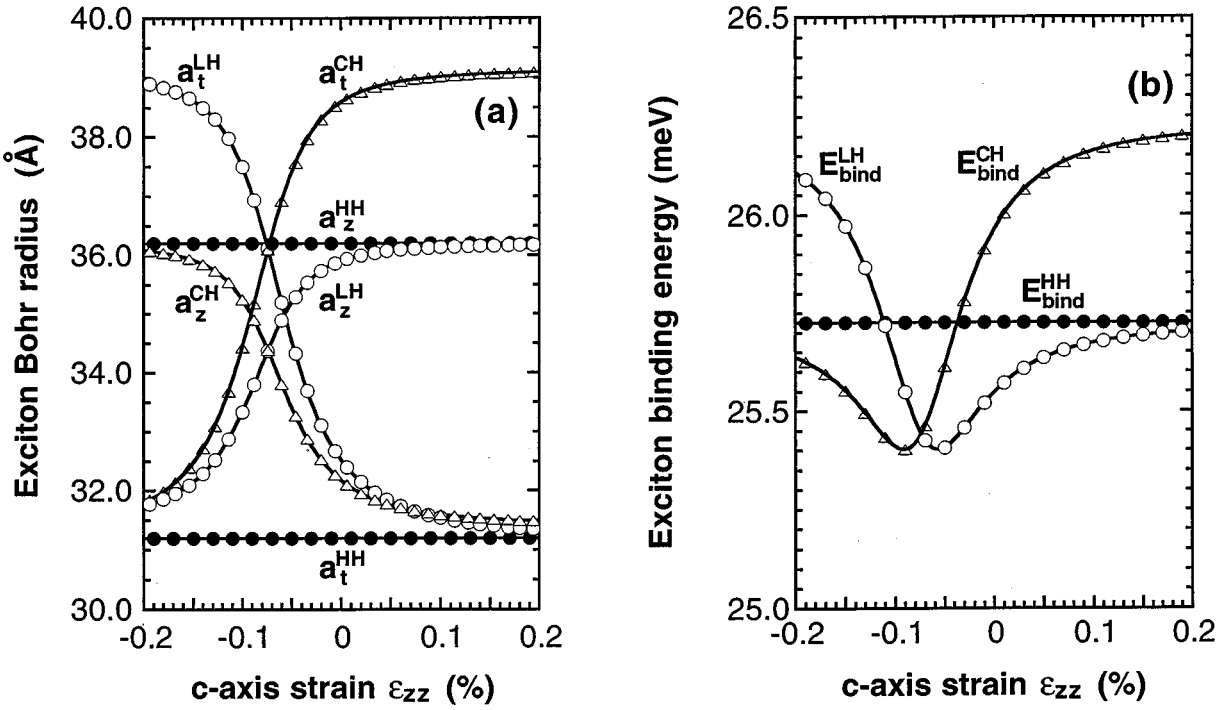

FIG. 10. (a) The exciton Bohr radius parameters a_t and a_z for the conduction band to HH, LH, and CH bands excitons and (b) their corresponding binding energies are plotted as a function of the c-axis strain.

edge optical properties and electronic transport issues using wurtzite GaN crystals.

ACKNOWLEDGMENTS

The authors would like to thank Dr. N. Uesugi for his continual encouragement. One of the authors (M.K.) gratefully acknowledges useful discussions with Dr. T. Takagahara.

APPENDIX: BASIS FUNCTIONS

The 6×6 valence band Hamiltonian for the strained wurtzite semiconductor takes 3×3 block diagonalized form when we introduce the following basis functions:

$$|1\rangle=-\frac{\alpha^*}{\sqrt{2}}|(X+iY)\uparrow\rangle+\frac{\alpha}{\sqrt{2}}|(X-iY)\downarrow\rangle,$$

$$|2\rangle=\frac{\beta}{\sqrt{2}}|(X-iY)\uparrow\rangle-\frac{\beta^*}{\sqrt{2}}|(X+iY)\downarrow\rangle,$$

$$|3\rangle=\beta^*|Z\uparrow\rangle+\beta|Z\downarrow\rangle,$$

$$|4\rangle=-\frac{\alpha^*}{\sqrt{2}}|(X+iY)\uparrow\rangle-\frac{\alpha}{\sqrt{2}}|(X-iY)\downarrow\rangle, \tag{A1}$$

$$|5\rangle=\frac{\beta}{\sqrt{2}}|(X-iY)\uparrow\rangle+\frac{\beta^*}{\sqrt{2}}|(X+iY)\downarrow\rangle,$$

$$|6\rangle=-\beta^*|Z\uparrow\rangle+\beta|Z\downarrow\rangle,$$

where

$$\alpha=\frac{1}{\sqrt{2}}\exp\left[i\left(\frac{3\pi}{4}+\frac{3\phi}{2}\right)\right], \tag{A2}$$

$$\beta=\frac{1}{\sqrt{2}}\exp\left[i\left(\frac{\pi}{4}+\frac{\phi}{2}\right)\right], \tag{A3}$$

and

$$\phi=\tan^{-1}\left(\frac{k_y}{k_x}\right). \tag{A4}$$

[1] S. Nakamura, T. Mukai, and M. Senoh, Jpn. J. Appl. Phys., Part 2 **30**, L1998 (1991).

[2] S. Nakamura, T. Mukai, and M. Senoh, Appl. Phys. Lett. **64**, 1687 (1994).

[3] G. L. Bir and G. E. Pikus, *Symmetry and Strain-Induced Effects in Semiconductor* (Wiley, New York, 1974).

[4] M. Suzuki, T. Uenoyama, and A. Yanase, Phys. Rev. B **52**, 8132 (1995).

[5] Yu. M. Sirenko, J. B. Jeon, K. W. Kim, M. A. Littlejohn, and M. A. Stroscio, Phys. Rev. B **53**, 1997 (1996).

[6] S. L. Chuang and C. S. Chang, Appl. Phys. Lett. **68**, 1657 (1996).

[7] S. L. Chuang and C. S. Chang, Phys. Rev. B **54**, 2491 (1996).

[8] J. M. Luttinger and W. Kohn, Phys. Rev. **97**, 869 (1955).
[9] A. Shikanai, T. Azuhata, T. Sota, S. Chichibu, A. Kuramata, K. Horino, and S. Nakamura, J. Appl. Phys. **81**, 417 (1997).
[10] *Handbook of Mathematical Functions*, edited by M. Abramowitz and I. A. Stegun (Dover, New York, 1970), p. 17, Eq. 3.8.2.
[11] S. Strite and H. Morkoç, J. Vac. Sci. Technol. B **10**, 1237 (1992).
[12] *Physics of Group IV Elements and III-V Compounds*, edited by K. H. Hellwege and O. Madelung, Landolt-Börnstein, New Series, Group III, Vol. 17, Pt. a (Springer-Verlag, Berlin, 1982).
[13] W. Shan, T. J. Schmidt, X. H. Yang, S. J. Hwang, and J. J. Song, Appl. Phys. Lett. **66**, 985 (1995).
[14] W. Shan, T. J. Schmidt, R. J. Hauenstein, and J. J. Song, Appl. Phys. Lett. **66**, 3492 (1995).
[15] A. Polian, M. Grimsditch, and I. Grzegory, J. Appl. Phys. **79**, 3343 (1996).
[16] R. W. Keyes, IBM J. Res. Dev. **5**, 65 (1961).